



Effect of Post-Heat Treatment on the Microstructure and Mechanical Properties of Laser-Deposited WxC + Ni-Based Composite Thin Walls

Chen Chen, Chengchao Du, Qihong Pan, and Qin Chen

Submitted: 16 June 2020 / Revised: 16 October 2020 / Accepted: 7 November 2020 / Published online: 24 November 2020

This paper reports the effect of post-heat treatment (PHT) on laser-deposited WxC + Ni-based composite thin walls. The PHT at 700, 800, and 900 °C was conducted to modify the microstructure and mechanical properties of the composite. The results showed that the as-deposited composite had a weak flexural strength and plasticity due to the brittle nature of the eutectic phase. The eutectic phase consisted of M₇C₃, M₂C, and a small amount of the γ phase. However, after PHT at a certain temperature (e.g., 700 or 800 °C), the eutectic phase gradually disappeared, and carbides, such as M₇C₃ and M₂C, tended to be distributed uniformly in the γ matrix, which improved the flexural strength of the composite. Nevertheless, after the PHT at 900 °C, the flexural strength of the composite displayed a downward trend, which was mainly because of the severe softening of the γ phase. In addition, the plasticity of this composite continuously improved as the eutectic phase disappeared and the γ phase softened. Based on the above results, we proposed a PHT at 800 °C for 1 h as an optimal process for this WxC + Ni-based composite.

Keywords flexural strength, heat treatment, laser deposition, Ni-based composite, plasticity

1. Introduction

WC is widely used as a reinforcement in Fe-based alloy (Ref 1), Ni-based alloy (Ref 2, 3), and Co-based alloy (Ref 4, 5). WC + Ni-based composites generally have the advantages of high hardness, high temperature resistance, and excellent wear resistance and have been widely used in mining machinery (Ref 6–9). Laser deposition is an effective way to fabricate composites. In recent years, composites reinforced by hBN (Ref 10), SiC (Ref 11), WC (Ref 2), MAX phase (Ref 12), and WS₂ (Ref 13) have been fabricated using laser deposition. Among them, the microstructure and mechanical of WC + Ni-based composites get a lot of attention (Ref 14, 15). It is known that the eutectic phase is a common phase in Ni-based alloys. In Inconel 718 superalloys, the eutectic phase is a mixture of the γ phase and Laves phase (Ref 16, 17). In NiCrBSi alloys, the eutectic phase is a mixture of the γ phase, carbides, and borides (Ref 18–21). The brittle nature of the Laves phase, carbides, and borides causes the brittle nature of the eutectic phase in Ni-based alloys. These investigations (Ref 22–24) showed that the eutectic phase is an essential factor for cracking formation. To eliminate the adverse effects of the eutectic phase, the microstructure of the eutectic phase should be modified.

Post-heat treatments (PHTs) are an effective way to modify the morphology of eutectics. Yu et al. (Ref 25, 26) observed the phase transformation of the Al₉(Mn, Ni)₂ eutectic phase in an Al-4Ni-2Mn alloy during heat treatment. The results showed that the Al-Ni-Mn κ -phase preferred to nucleate at the interface between the Al matrix and the Al₉(Mn, Ni)₂ eutectic phase and then grew into the parent phase, which resulted in the breakup of the eutectic fibers at the nucleation sites. Guo et al. (Ref 27) found that the eutectic phase (γ -phase + Laves) in an Inconel 718 alloy was eliminated by the holding process after deformation. The fraction of the eutectic phase decreased from 5.35 to 2.53 vol.% after 2 min of holding at 1170 °C. Therefore, a PHT might be an effective way to modify the eutectic phase.

In this investigation, a WC/W₂C (WxC)-reinforced Ni-based composite with high hardness and wear resistance was fabricated using laser deposition. A continuous eutectic phase was observed in the Ni-based matrix. To reduce the adverse effects from the eutectic phase, a PHT was employed. Microstructure observations, hardness tests, and three-point bending tests were performed, and the effect of the modified microstructure on the mechanical properties was determined and is discussed.

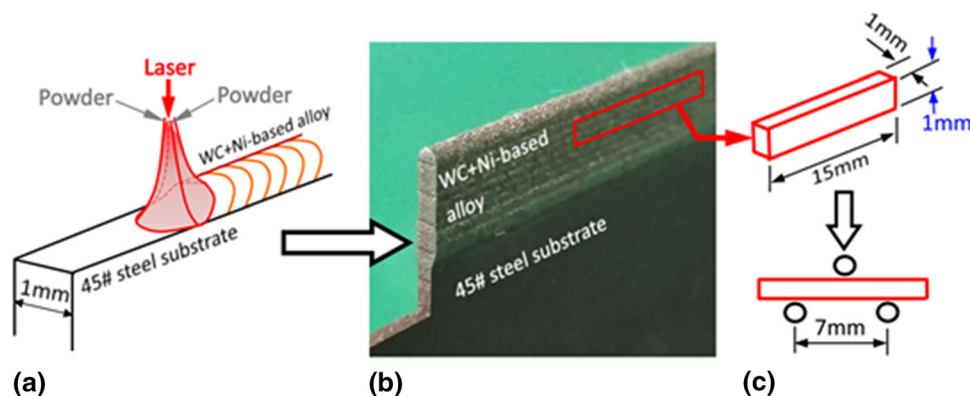
2. Materials and Experiments

The diameter of the Ni-based powder was between 20 μ m and 50 μ m. The chemical composition of the original Ni-based alloy powder is shown in Table 1. A cast WxC particle with an average diameter of 60 μ m was employed. The fraction of WC in the WxC powder was approximately 44 mol.%. The two powders (Ni-based powder and WxC powder) were mechanically mixed. The volume fraction of WxC in the mixture was 30%. A Trumpf disk 6002 laser generator was employed. A schematic of the laser deposition process is shown in Fig. 1(a).

Chen Chen, Chengchao Du, and Qihong Pan, School of Materials Science and Engineering, Jiangsu University, Zhenjiang 212013, China; and Qin Chen, Zhenjiang Technician Institute, Zhenjiang 212013, China. Contact e-mail: dccmaterials@ujs.edu.cn.

Table 1 Chemical composition of original Ni-based alloy powder, wt.%

	Cr	W	Si	C	Ni
Original Ni-based alloy powder	5.5-6.5	8.5-11.3	2.5-3.0	2.2-2.4	Bal

**Fig. 1** (a) Schematic of laser depositing process, (b) macro morphology of W_xC/Ni-based composite, (c) bending sample

The feeding system ejected the mixed powder to the convergent point. The convergent point was just under the laser beam. The powder melted at the convergent point, fell on the substrate, and formed the W_xC + Ni-based composite. The laser power, feeding speed, and deposition rate were 1.8 kW, 8 g/min, and 15 mm/s, respectively. The chemical composition of the deposited Ni-based alloy matrix was measured using electron probe microanalysis (EPMA, Shimadzu EPMA-1720) and is shown in Table 1. The macromorphology of the as-deposited W_xC + Ni-based composite is shown in Fig. 1(b).

The PHT was conducted in a muffle furnace. The PHT temperatures were chosen as 700, 800, and 900. The PHT time was set as 1 h. During the PHT, the samples were placed in a quartz tube filled with Ar gas. After the PHT, the samples were cooled in air. The cross sections of the composites were ground and finally polished using oxide polishing suspensions. Then, the cross sections were etched using aqua regia. The microstructure and fractured surface of the W_xC + Ni-based composite were observed using scanning electron microscopy (SEM, TESCAN MIRA, FEI NovaNano450). The element distribution of the W_xC + Ni-based composite was analyzed using EPMA. The composition of the W_xC + Ni-based composite was analyzed using energy dispersive spectroscopy (EDS, Oxford). The phases of the W_xC + Ni-based composite were analyzed using x-ray diffraction (XRD, Rigaku Smartlab 9 kW, copper target, 48 kV/100 mA). Samples with dimensions of 5 mm × 5 mm × 1 mm were machined from the composites for XRD analysis. The surface with dimensions of 5 mm × 5 mm was finally ground using 2000-grit sandpaper. The samples were scanned from 20° to 80°. The scanning speed was 2°/min. The phase transformation diagram was calculated using JMatPro software (Version 6.0). The “Nickel Based Superalloy” database was chosen. A temperature range from 600 to 1500 °C was set. The chemical compositions of three regions in the Ni-based matrix in the composite were measured using EPMA. The results are shown in Table 2. This result indicated that the average composition of C reached the maximum value in the original Ni-based composite alloy.

Table 2 Chemical composition of Ni-based matrix of composite and Ni-based alloy for phase diagram calculation, wt.%

	Cr	W	Si	C	Ni
Region 1	5.8	11.2	2.9	2.5	Bal
Region 2	5.6	10.2	2.9	2.3	Bal
Region 3	6.4	9.3	2.5	2.5	Bal
Average	5.9	10.2	2.8	2.4	Bal
Ni-based for phase diagram calculation	6	10	2.8	2.3	Bal

Therefore, considering the error associated with EPMA results, the chemical composition was revised based on the original Ni-based alloy powder. The chemical composition for the phase diagram calculation is shown in Table 2. The three-point bending test was conducted with the help of a fixture, as shown in Fig. 1(c). The samples were tested with a loading rate of 0.1 mm/min at room temperature and under normal humidity conditions. The flexural strength was calculated according to Eq 1 (Ref 28). The hardness was measured using a microhardness tester (FM-ARS900) with a load of 200 g.

$$\sigma = (3 * F * L) / (2 * b * h * h) \quad (\text{Eq 1})$$

where F is the maximum load, L is the span of the fixture, b is the width of the sample, and h is the thickness of the sample.

3. Results and Discussion

3.1 Results

3.1.1 Microstructure of the as-Deposited Composite. The cross-sectional macromorphology of the as-deposited W_xC + Ni-based composite is shown in Fig. 2(a). The microstructure of the region marked in Fig. 2(a) is shown in

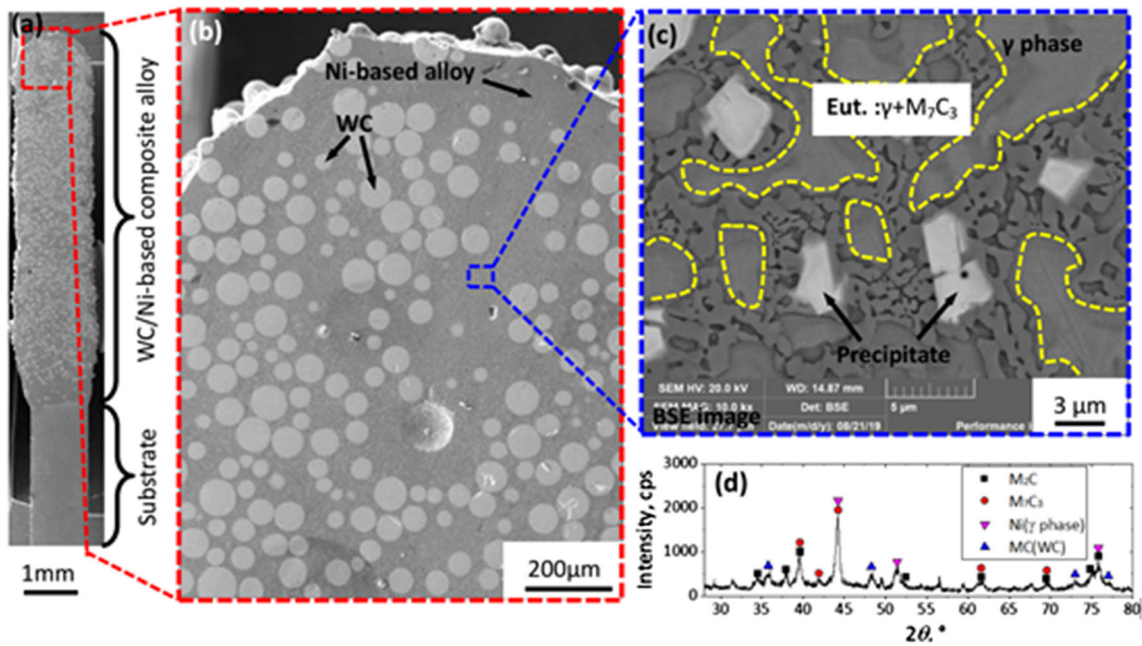


Fig. 2 Microstructure of as-deposited W_xC + Ni-based composite: (a) macro morphology, (b) micro morphology, (c) Ni-based matrix, (d) XRD pattern

Fig. 2(b). A spherical cast W_xC particle and the Ni-based alloy matrix are indicated in Fig. 2(b). According to five optical images of the as-deposited composite, the volume fraction of W_xC was between 25 and 36%. This result indicated that the W_xC particles were uniformly distributed in the composite. The microscale region of the Ni-based matrix marked in Fig. 2(b) is shown in Fig. 2(c). The microstructure of the Ni-based matrix consisted of the γ phase and eutectic phase. The boundary of the two phases is indicated as the yellow line in Fig. 2(c). The XRD pattern of the as-deposited W_xC + Ni-based composite is shown in Fig. 2(d). M_2C , M_7C_3 , γ phase, and MC were observed in the as-deposited composite.

The phase transformation diagram of the Ni-based matrix is shown in Fig. 3(a) and (b). The primary M_2C precipitated from the liquid at 1395 °C, as shown in Fig. 3(a). The primary γ phase precipitated at 1269 °C, as shown in Fig. 3(b). When the temperature decreased to 1246 °C, the primary γ phase completely precipitated from the liquid. The DSC curve of the Ni-based alloy during heating is shown in Fig. 3(c). At a temperature of approximately 1250 °C, the eutectic phase started to transform into a liquid. Between 1250 and 1281 °C, the primary γ phase gradually transformed into a liquid. As there was a low fraction of M_2C , the endothermic dissolution of the M_2C was not remarkable. According to the DSC curve, the calculated result of the Ni-based matrix was credible.

The eutectic transformation occurred at 1246 °C. The retained liquid directly formed the eutectic phase (secondary γ phase and M_7C_3). At this temperature, M_2C should rapidly decompose into M_7C_3 and MC. However, the primary M_2C remained until room temperature was reached due to the high cooling speed of the laser deposition process. According to the volume fraction of M_7C_3 and primary M_2C , the white precipitate in Fig. 2(c) was M_2C . The eutectic phase consisted of the secondary γ phase and M_7C_3 , as indicated in Fig. 2(c).

The chemical compositions of M_7C_3 and M_2C are shown in Fig. 3(d). The M_7C_3 comprised a (Ni, Cr)-rich phase. The M_2C comprised a (Cr, W)-rich phase. The element distributions in

the region in Fig. 4(a) (as-deposited sample) are shown in Fig. 4(b)–(f). From the distributions of Ni and W, the white M_2C phase in the BSE image was confirmed. The EDS patterns from the M_7C_3 and M_2C are shown in Fig. 4(g) and (h). The results from EDS were similar to those from EPMA.

Based on the above results and discussion about the microstructure of the Ni-based matrix, the solidification process of the Ni-based matrix was determined, as shown in Fig. 5. The primary M_2C gradually precipitated from the liquid between 1395 and 1269 °C, as shown in Fig. 5(a). Between 1269 and 1246 °C, the primary γ phase and primary M_2C precipitated together, as shown in Fig. 5(b) and (c). When the temperature decreased to 1246 °C, the retained liquid phase transformed into the eutectic phase directly, as shown in Fig. 5(d).

3.1.2 Microstructure After the PHT. After the PHT, the eutectic phase gradually disappeared, as shown in Fig. 6(a)–(c). The microstructure consisted of the γ phase, M_7C_3 , and M_2C after the PHT at temperatures of 700 and 800 °C. After the PHT at 900 °C, a small number of precipitates with a lower contrast was generated, as indicated in Fig. 6(f).

The disappearance of the eutectic phase was common during the PHTs. According to Fig. 2(c), the irregular M_7C_3 phase was observed in the eutectic. Many interfaces between the M_7C_3 and γ phases were observed in the eutectic phase. This contributed to the high interface energy of the as-deposited composite. During the PHTs, the interface energy tended to decrease. Therefore, the irregular M_7C_3 changed to reduce the interface energy. In the as-deposited sample, M_7C_3 was only in the eutectic phase. The M_7C_3 in the composite heat-treated at 900 °C was uniformly distributed in the γ phase matrix. The redistribution of the elements in M_7C_3 was element diffusion during the PHT. In the as-deposited composite, Cr, W, and C were segregated in the eutectic phase. During PHT, these elements gradually diffused to the primary γ phase and contributed to the homogenization of the carbides.

In the as-deposited W_xC + Ni-based composite, the microstructure at high temperatures was retained to room

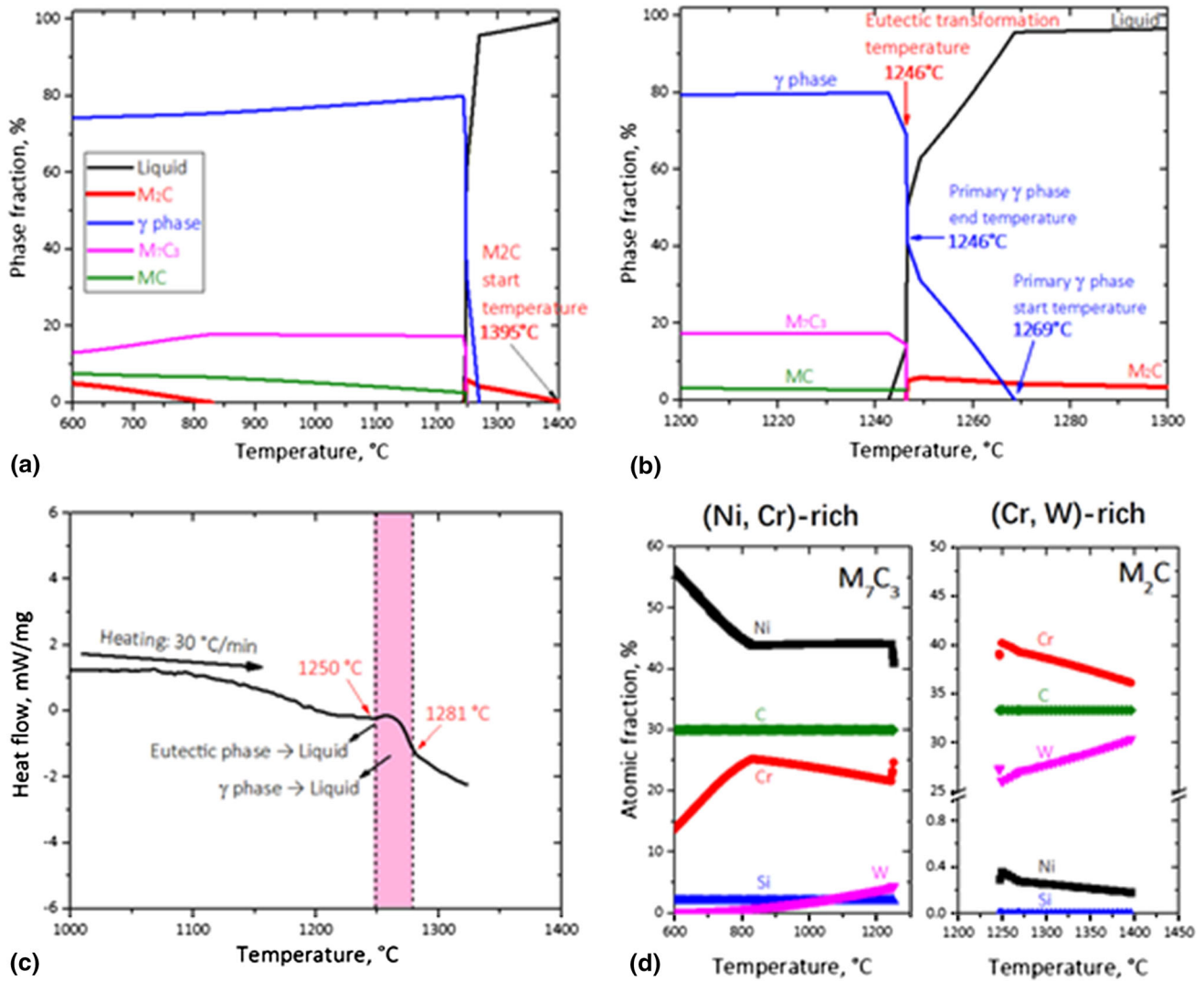


Fig. 3 (a) and (b) Phase diagram of Ni-based matrix, (c) DSC curve of Ni-based matrix, (d) Chemical compositions of M_7C_3 and M_2C as a function of temperature

temperature at a high cooling speed. The phase fractions of M_7C_3 , MC, and M_2C were calculated using JMatPro software and are listed in Table 3. The phase fraction of the Ni-based alloy at 1246 °C was chosen to represent the microstructure of the as-deposited Ni-based matrix. The phase fraction of M_7C_3 was between 15.0 and 18.1 vol.%. The M_7C_3 fraction of the three composites measured from the BSE images was approximately 19 vol.%. It was concluded that the PHT did not remarkably change the fraction of M_7C_3 . The phase fraction of M_2C gradually decreased as the PHT temperature increased.

It was observed that the MC precipitates existed at the three temperatures. Therefore, the MC precipitates were gradually generated during the PHT. The MC precipitates always had a low contrast due to their high carbon fraction. Therefore, they were identified, as shown in Fig. 6(f). According to the difference in contrast in the BSE image, the MC phase was not observed in the composites that underwent PHTs at 700 and 800 °C. The MC phase with a fraction of 3.1 vol.% was observed in the composite that underwent the PHT at 900 °C.

The reduction in M_2C and increase in MC indicated that the M_2C precipitates were gradually transformed into MC precipitates

at 900 °C. This phase transformation relied on atomic diffusion. A lower temperature contributed to slower atomic diffusion. The generation of MC precipitates at temperatures of 700 and 800 °C was harder than that at 900 °C. Therefore, MC precipitates were not observed in the $W_xC + Ni$ -based composite heat-treated at temperatures of 700 and 800 °C.

During the PHTs, the microstructure of the γ phase also slightly changed. The XRD patterns of the as-deposited and $W_xC + Ni$ -based composites that underwent a PHT are shown in Fig. 7(a). The angles of the three peaks from the γ phase are shown in Fig. 7(b). It was observed that the angles of the three peaks gradually increased and were close to the standard angle for pure Ni. The shift of the peaks was attributed to the solid solution atom diffusion from the γ phase to the precipitates.

The atomic fraction of the γ phase as a function of temperature was calculated using JMatPro software and is shown in Fig. 7(c). The fractions of Cr, W, and C gradually declined as the temperature decreased. Regarding the as-deposited alloy, the Cr fraction was 3.61 at.%. The Cr fraction declined to 1.77, 1.38, and 0.96 at.% at temperatures of 900, 800, and 700 °C, respectively. The Cr fraction of the γ phase was measured using EDS, as shown in Fig. 7(d). The lowest Cr

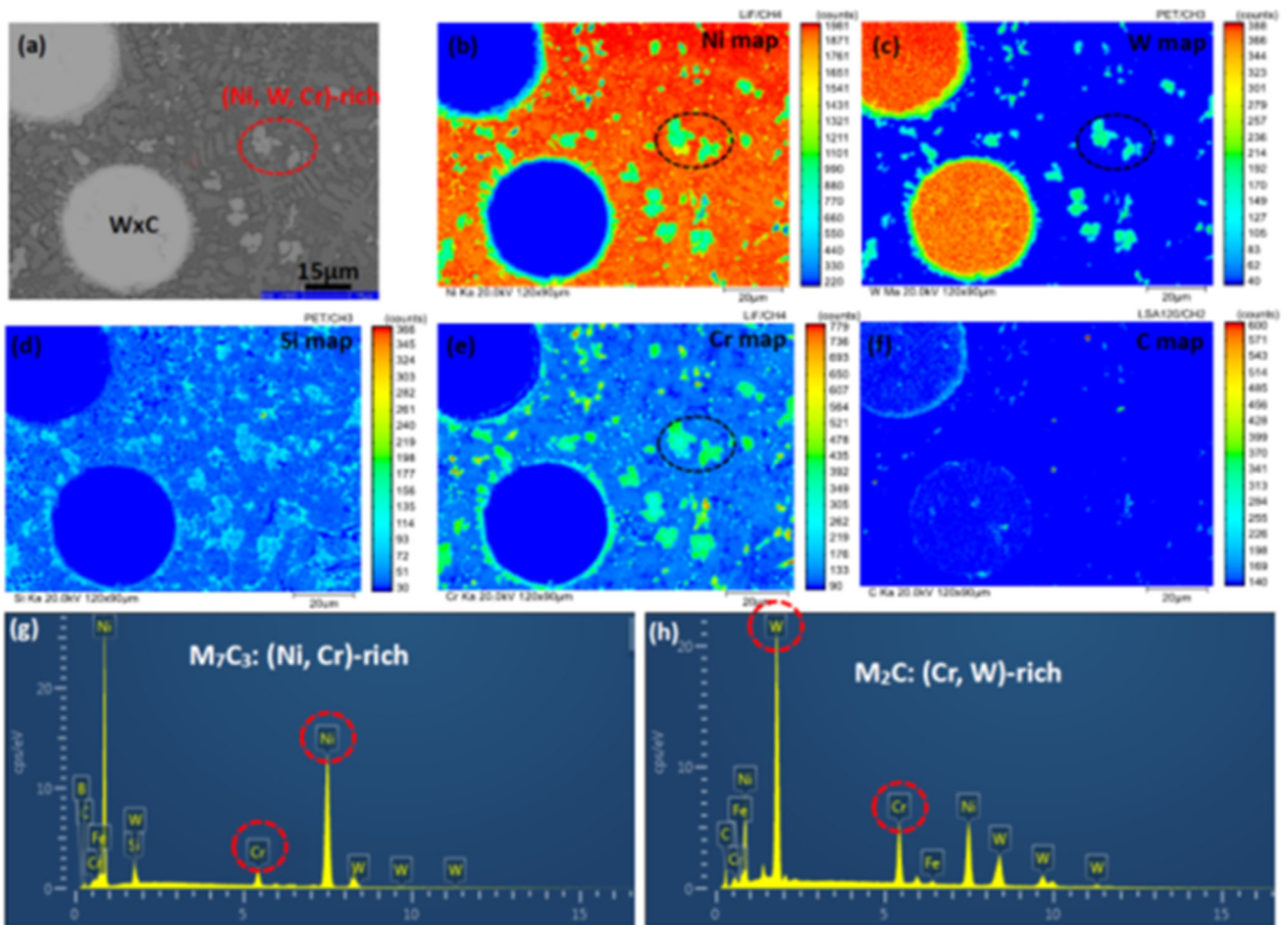


Fig. 4 (a) BSE image of composite, (b) Ni map, (c) W map, (d) Si map, (e) Cr map, (f) C map, (g) EDS pattern of M_7C_3 , (h) EDS pattern of M_2C

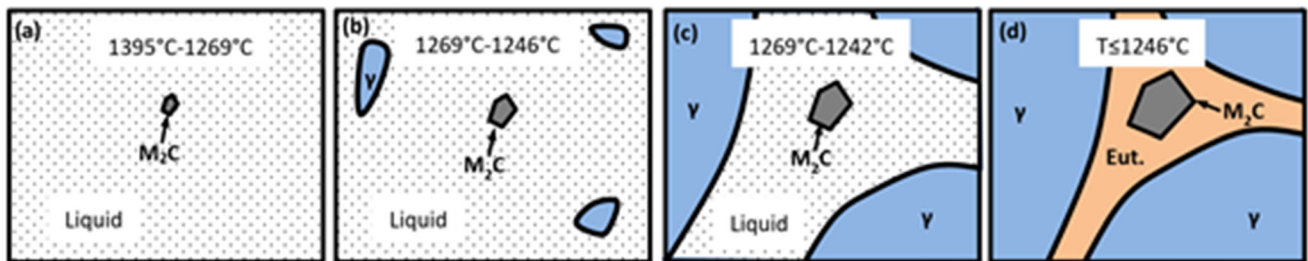


Fig. 5 Solidification procedure: (a) 1395-1269 °C, (b) and (c) 1269-1246 °C, (d) \leq 1246 °C

fraction of approximately 2.63 at.% was observed in the γ phase after heat treatment at 900 °C.

The reduction in the number of solid solution atoms depended on the diffusion of these atoms during the PHT. The temperature remarkably affected the diffusion rate of these solid solution atoms. The solid solution atoms at 900 °C had the fastest diffusion among the PHT temperatures. Therefore, the γ phase after PHT at 900 °C had the smallest fraction of solid solution atoms.

3.1.3 Hardness, Flexural Strength, and Plasticity. The hardness of the Ni-based matrix is shown in Fig. 8. It gradually declined from 653 HV to 552 HV as the PHT temperature increased. The hardness of the Ni-based matrix was higher than that of a standard Ni45 alloy (Ref 29). According to the

hardness (2124 HV) and volume fraction (30%) of the W_xC particles, the hardness of the as-deposited W_xC + Ni-based composite was approximately 903 HV. After a PHT at 900 °C, the hardness of the W_xC + Ni-based composite declined to approximately 832 HV.

The flexural strength and ultimate displacement as a function of PHT temperature are shown in Fig. 9. The sample that underwent PHT at 800 °C achieved the maximum flexural strength (704 MPa). The ultimate displacement increased as the PHT temperature increased. This indicated that the composite exhibited excellent flexural strength when heated at 800 °C for 1 h. The plastic deformation ability of the composite gradually improved as the heating temperature increased.

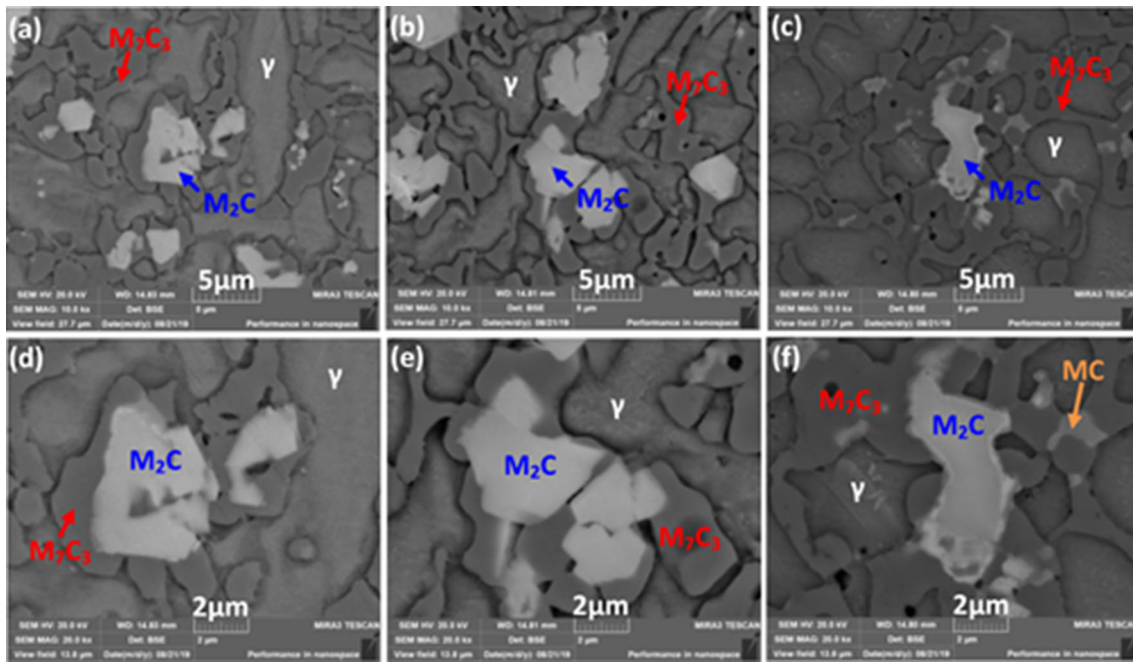


Fig. 6 Microstructure of PHTed Ni-based matrix: (a) and (d) at 700 °C, (b) and (e) at 800 °C, (c) and (f) at 900 °C

Table 3 Phase fraction at 700, 800, and 900 °C, vol.%

Phase	M ₇ C ₃		M ₂ C		MC	
	Calculated	Measured	Calculated	Measured	Calculated	Measured
As-deposited at 1246 °C	18.1	19.4 ± 1.7	6.3	8.8 ± 2.5	0	0
700 °C	15.0	19.2 ± 2.1	3.1	8.3 ± 1.7	7.1	0
800 °C	17.0	18.7 ± 1.9	0.6	7.9 ± 0.8	6.7	0
900 °C	17.8	19.3 ± 1.6	0	6.2 ± 1.4	6.1	3.1 ± 1.1

3.2 Discussion

3.2.1 Softening Mechanism of the Composite after PHT. The hardness decline of the Ni-based matrix was attributed to the weakening of the strengthening effect. According to Table 3, the total volume fraction of M₇C₃, M₂C, and MC was approximately 27 vol.% and was not remarkably changed during PHT. Therefore, the strengthening effect provided by the hard phase was roughly stable during PHT. The composite did not experience plastic deformation. Therefore, the strengthening effect provided by dislocations was also roughly stable during PHT. During the PHT process, the grains should grow. High temperatures contributed to rapid grain growth. The coarse grains contributed to the weakening of the strengthening effect from the grain boundaries (Ref 30, 31). According to the reduction in the solid solution atoms in the γ phase, the solid solution strengthening effect of the γ phase decreased during PHT (Ref 32). Therefore, the hardness decline of the Ni-based matrix was attributed to grain growth and a reduction in the number of solid solution atoms in the γ phase.

3.2.2 Fracture Behavior of the Composites. The fracture surface of the as-deposited composite is shown in Fig. 10. The SE images are shown in Fig. 10(a) and (c). The BSE images are shown in Fig. 10(b) and (d)–(f). According to Fig. 10(a)–(c), brittle fracture of the WC particles, M₂C, and M₇C₃ was observed.

In the as-deposited composite, the γ phase was considered the only phase that could undergo plastic deformation. Therefore, the torn edge on the fracture surface was due to plastic deformation of the γ phase. Two types of tear edges with different widths were observed in Fig. 10(b) and (e). According to Fig. 10(e) and (f), a narrow tear edge was found between the M₇C₃ phase, as shown in Fig. 10(f). In the as-deposited composite, the eutectic phase consisted of M₇C₃ and the secondary γ phase. The fine secondary γ phase was between the continuous M₇C₃ precipitates. Therefore, the plastic deformation of the secondary γ phase in the eutectic phase contributed to the narrow tear edge in Fig. 10(e).

In Fig. 10(b) and 11(a), a wide tear edge is indicated. The formation of a wide tear edge was dependent on the plastic deformation of the coarse γ phase. The primary γ phase in the as-deposited composite is shown in Fig. 11(b). A coarsened γ phase surrounded by the eutectic phase was observed. During the bending test, the plastic deformation of the primary γ phase contributed to the formation of a wide tear edge.

Based on the above discussion, the fracture of the as-deposited composite depended on two factors: (a) brittle fracture of WC, M₂C, and M₇C₃; and (b) ductile fracture of the primary γ phase and secondary γ phase. In the as-deposited composite, the plastic deformation ability of the γ phase was limited due to the increased solid solution strengthening effect.

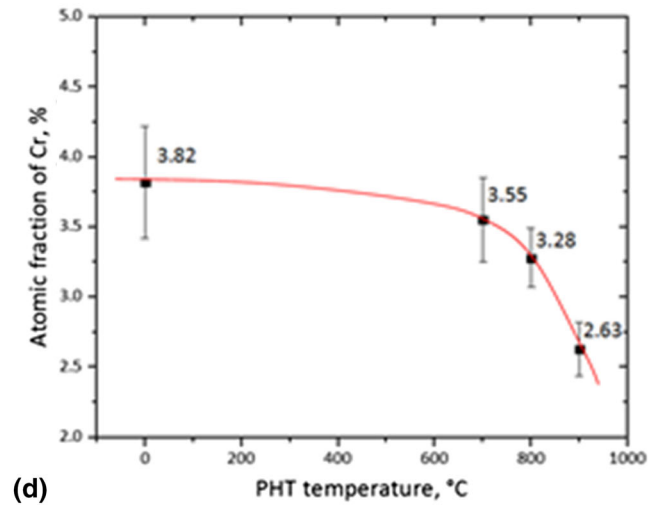
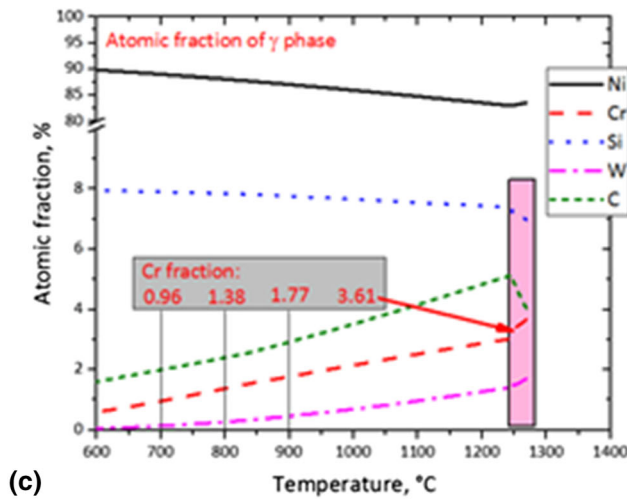
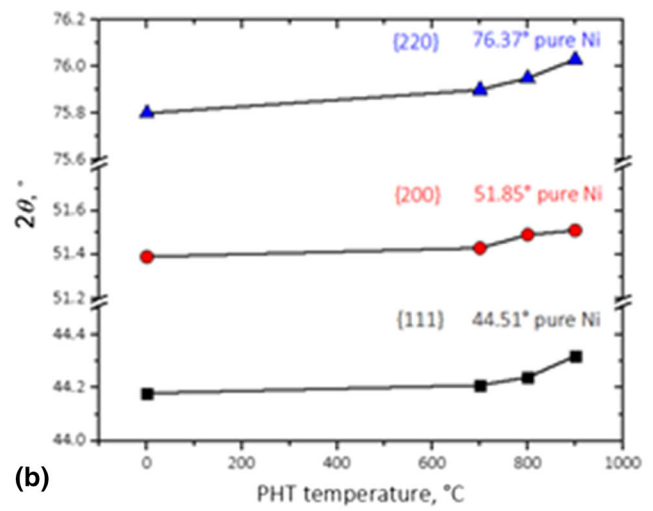
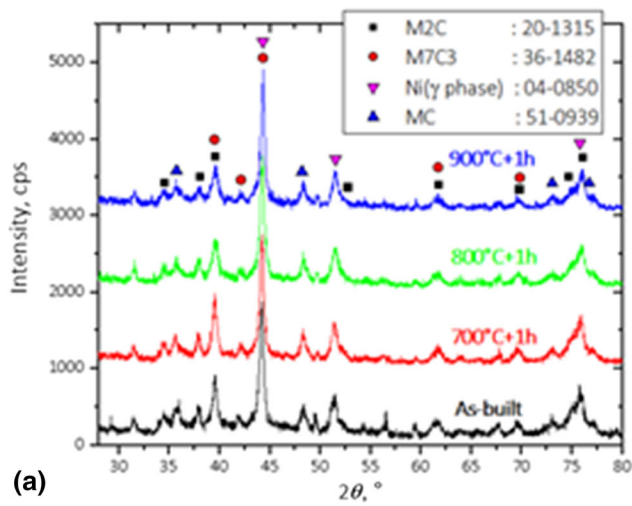


Fig. 7 (a) XRD patterns, (b) Angle of three peaks of γ phase, (c) Composition of γ phase as a function of temperature, (d) Atomic fraction of Cr as a function of PHT temperature

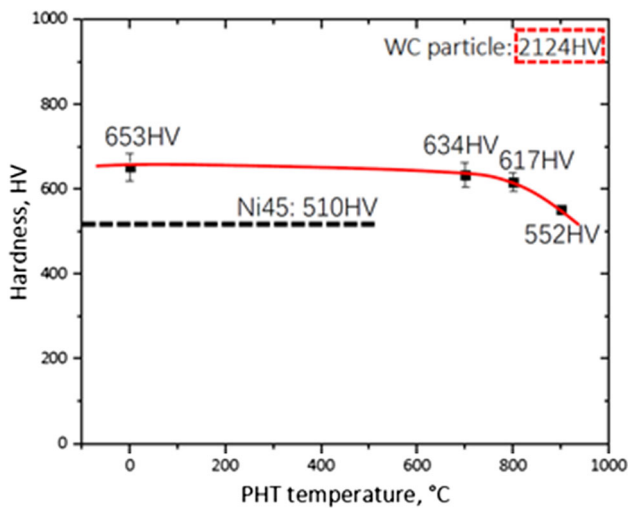


Fig. 8 Hardness of Ni-based matrix as a function of PHT temperature

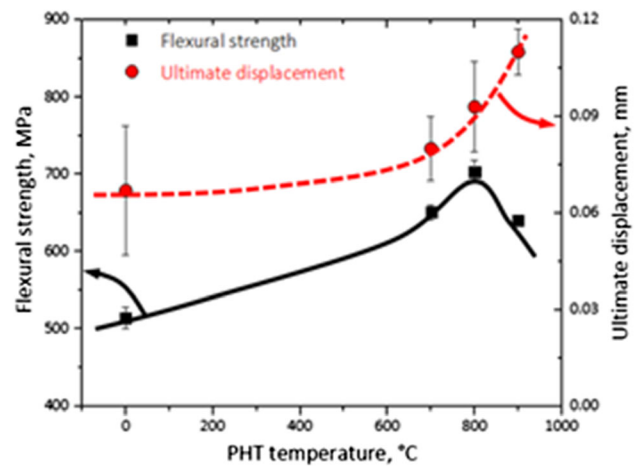


Fig. 9 Flexural strength and ultimate displacement as a function of PHT temperature

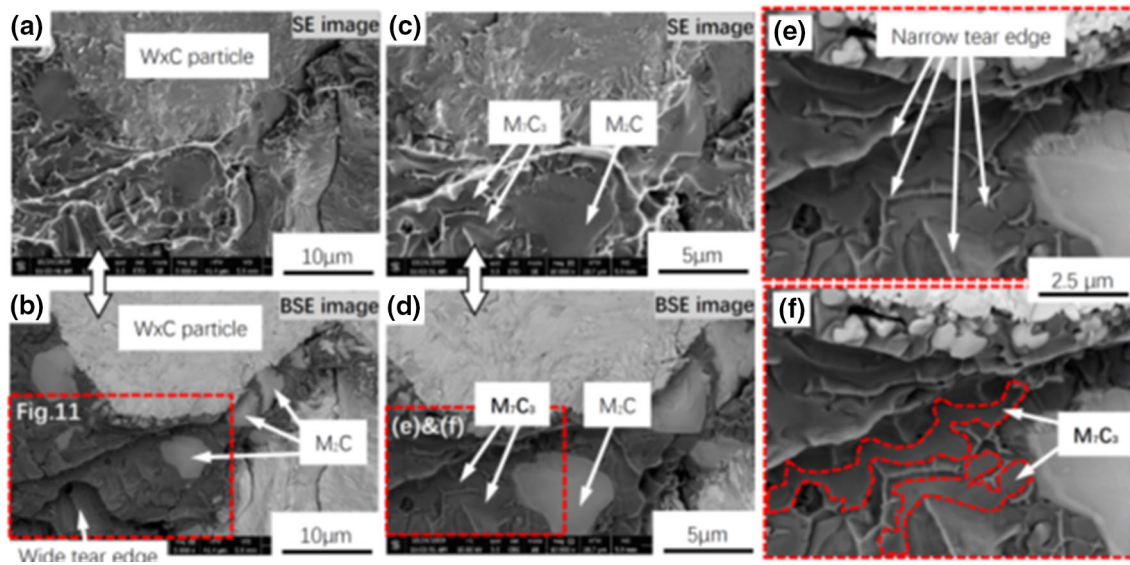


Fig. 10 Fracture surfaces of as-deposited WxC + Ni-based composite: (a) and (c) SE images; (b), (d), (e), and (f) BSE images

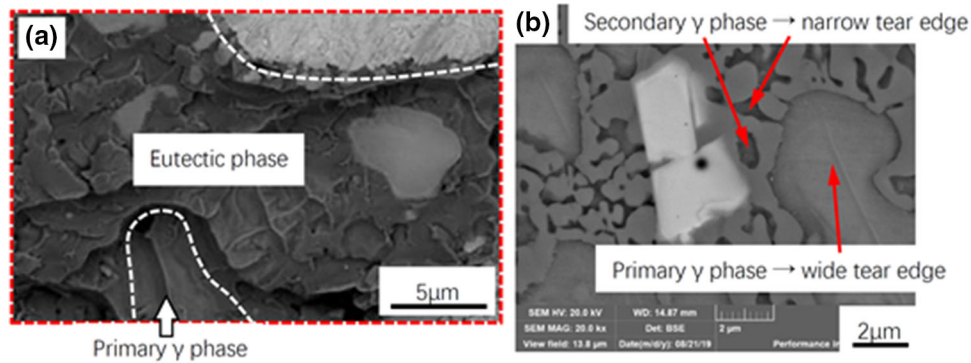


Fig. 11 (a) Fracture surface as indicated in Fig. 10, (b) microstructure of as-deposited composite

Therefore, dimples were not observed on the fracture surface. The eutectic phase induced crack propagation due to its high fraction of M_7C_3 and M_2C .

The fracture surfaces of the composite PHT at 700 °C are shown in Fig. 12(a) and (b). A similar result to the that for the as-deposited composite was observed for the fracture surfaces. After PHT at 800 °C, the brittle fracture of WxC, M_2C , and M_7C_3 was still observed in Fig. 12(c) and (d). The continuous fracture of M_7C_3 was not observed on the fracture surface. According to Fig. 6(b) and (e), the continuous M_7C_3 in the as-deposited composite was modified. The coarsened γ phase between the M_7C_3 precipitates was observed. Therefore, the continuous fracture of M_7C_3 was restricted.

The wide tear edge is indicated in Fig. 12(c) showed ductile fracture of the coarse γ phase. Moreover, dimples were observed on the fracture surface, as shown in Fig. 12(e). This meant that the plastic deformation ability of the γ phase in the composite that underwent PHT at 800 °C was enhanced.

The fracture surfaces of the composite that underwent PHT at 900 °C are shown in Fig. 13. According to the SE images [Fig. 13(a) and (c)] and BSE images [Fig. 13(b) and (d)], brittle fracture of WxC, M_2C , and M_7C_3 was observed. According to Fig. 13(e), a remarkable dimpling was observed. In the

composite that underwent PHT at 900 °C, the coarse γ phase was surrounded by M_7C_3 , as shown in Fig. 6(c). During the bending test, the coarsened γ phase experienced severe plastic deformation and contributed to the formation of dimples. The formation of dimples also indicated an improved plastic deformation ability of the γ phase in the composite that underwent PHT at 900 °C.

Based on the above discussion, the fracture of the composite that underwent PHT at 900 °C depended on two factors: (a) brittle fracture of WC, M_2C , and M_7C_3 ; and (b) ductile fracture of the γ phase. In the composite that underwent PHT, the plastic deformation ability of the γ phase was enhanced as the solid solution strengthening effect weakened. Therefore, dimples were observed on the fracture surface. The eutectic phase disappeared and no longer induced crack propagation.

3.2.3 Enhancing Mechanism of Bending Properties. A higher hardness always contributes to a higher strength. However, the highest hardness of the as-deposited composite did not contribute the highest flexural strength in this investigation. This was attributed to the continuous eutectic phase. The eutectic phase, which has a high fraction of brittle M_7C_3 and M_2C , contributed to crack initiation and propagation during the bending test. After PHT at 700 and 800 °C, the continuous

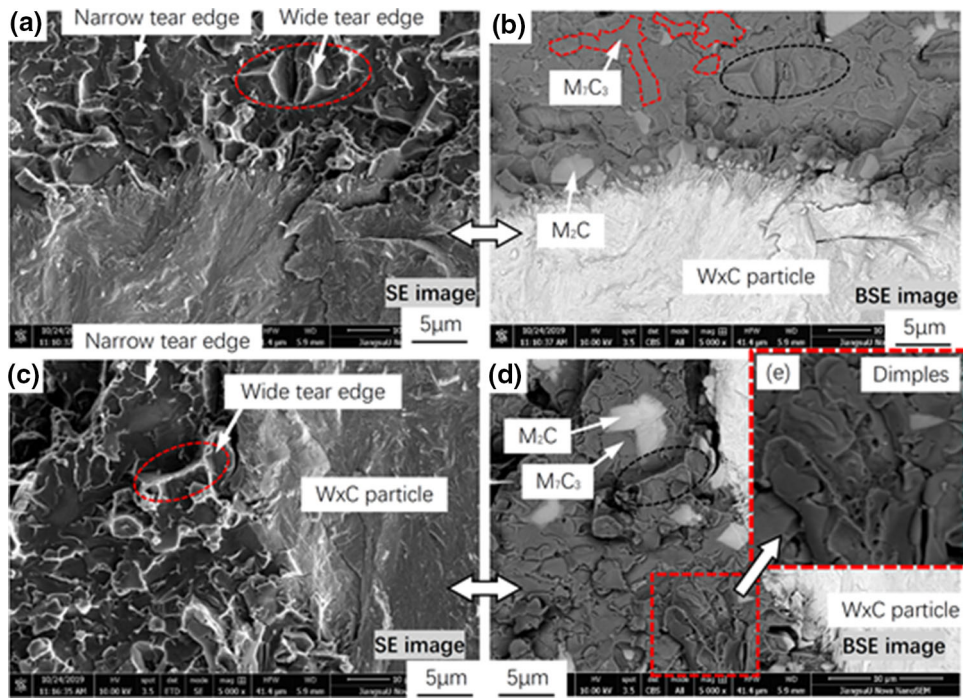


Fig. 12 (a) and (b) Fracture surfaces of composite heat-treated at 700 °C, (c)–(e) Fracture surfaces of composite heat-treated at 800 °C

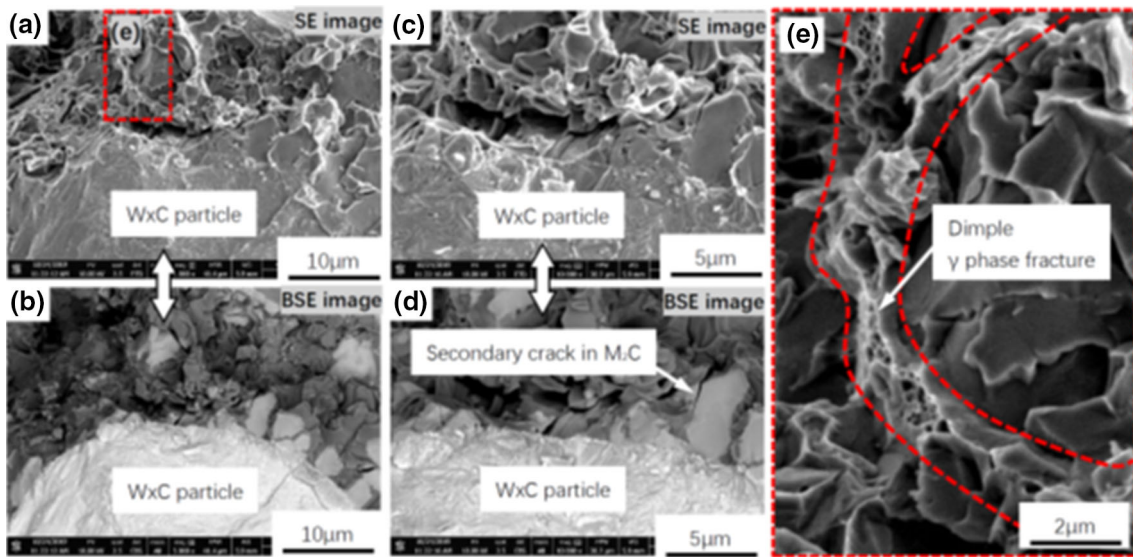


Fig. 13 Fracture surfaces of composite heat-treated at 900 °C: (a) and (c) SE images; (b), (d), and (e) BSE images

eutectic phase gradually disappeared. Therefore, the flexural strength increased to 704 MPa (800 °C) from 515 MPa (as-deposited composite). When PHT at 900 °C, remarkable softening of the γ phase occurred. The hardness of the Ni-based matrix declined to 552 HV. The poor strengthening of the γ phase contributed to the decrease in the flexural strength compared with that for the composite that underwent PHT at 800 °C.

The ultimate displacement depended on the plastic deformation ability of the composite. Regarding the as-deposited composite, the cracking of the eutectic phase limited the plastic deformation. After PHT, the eutectic phase gradually disappeared. The ultimate displacement improved. Moreover, the softening of the γ phase also contributed to the plastic

deformation ability of the composite after PHT. The gradually enhanced plastic deformation ability of the γ phase contributed to the transformation from the formation of tear edges to dimples on the fracture surfaces.

4. Conclusions

1. The thermodynamic calculations based on JMatPro software indicated that during the cooling stage of the WxC + Ni-based composite, M_2C precipitated from the

liquid at 1395 °C. The primary γ phase started precipitating at 1269 °C. When the temperature declined to 1246 °C, the primary γ phase completely precipitated from the liquid with a volume fraction of 41%. The residual liquid rapidly transformed into the eutectic phase. The primary M_2C in the eutectic phase was retained at room temperature at a high cooling speed.

2. After the PHT process, the eutectic phase gradually disappeared. M_7C_3 and M_2C were gradually uniformly distributed in the Ni-based matrix. After PHT at 900 °C, a small amount of MC was generated. The reduction in the number of solid solution atoms in the γ phase was increased progressively as the PHT temperature increased.
3. The hardness of the Ni-based matrix gradually declined as the PHT temperature increased. This trend was due to coarsening of the grains and a reduction in the number of solid solution atoms in the γ phase.
4. The flexural strength of the samples heat-treated at 700 and 800 °C continuously increased as the eutectic phase disappeared. The decline in the flexural strength of the sample that underwent PHT at 900 °C was attributed to the substantial softening of the Ni-based matrix.
5. The bending displacement of the samples continuously increased as the PHT temperature increased. The disappearance of the eutectic phase and softening of the γ phase contributed to the improvement in the plastic deformation ability of the Ni-based matrix together.

Acknowledgments

The authors would like to express their gratitude for projects supported by the National Key R&D Program of China (Grant No. 2019YFC0810704). In addition, all authors are particularly grateful to the medical staff who have fight against the COVID-19 for providing us with a safe research environment.

References

1. J.Z. Lu, J. Cai, H.F. Lu et al., Wear Properties and Microstructural Analyses of Fe-Based Coatings with Various WC Contents on H13 Die Steel by Laser Cladding, *Surf. Coat. Technol.*, 2019, **369**, p 228–237
2. R. Zhou, G.F. Sun, A.X. Feng et al., Effects of Yttrium on the Microstructure and Wear Properties of Laser-Aided Direct Metal Deposition (DMD) Co-285 + WC Coatings, *Lasers Eng.*, 2015, **31**, p 161–178
3. S. Hong, Y. Wu, J. Wu et al., Effect of flow Velocity on Cavitation Erosion Behavior of HVOF Sprayed WC-10Ni and WC-20Cr3C2-7Ni Coatings, *Int. J. Refract. Met. Hard Mater.*, 2020, **92**, p 105330
4. G.F. Sun, K. Wang, R. Zhou et al., Effect of Annealing on Microstructure and Mechanical Properties of Laser Deposited Co-285 + WC Coatings, *Opt. Laser Technol.*, 2015, **66**, p 98–105
5. D. Shu, Z. Li, K. Zhang et al., In Situ Synthesized High Volume Fraction WC Reinforced Ni-Based Coating by Laser Cladding, *Mater. Lett.*, 2017, **195**, p 178–181
6. E.O. Correa, J.N. Santos, and A.N. Klein, Microstructure and Mechanical Properties of WC Ni-Si Based Cemented Carbides Developed by Powder Metallurgy, *Int. J. Refract. Met. Hard Mater.*, 2010, **28**, p 572–575
7. E. Hao, X. Zhao, Y. An et al., WC-Co Reinforced NiCoCrAlYTa Composite Coating: Effect of the Proportion on Microstructure and Tribological Properties, *Int. J. Refract. Met. Hard Mater.*, 2019, **84**, p 104978
8. M. Zhang, M. Li, J. Chi et al., Effect of Ti on Microstructure Characteristics, Carbide Precipitation Mechanism and Tribological Behavior of Different WC Types Reinforced Ni-based Gradient Coating, *Surf. Coat. Technol.*, 2019, **374**, p 645–655
9. J. Škamat, O. Černašćus, Ž. Čepukē et al., Pulsed Laser Processed NiCrFeCSiB/WC Coating Versus Coatings Obtained Upon Applying the Conventional Re-melting Techniques: Evaluation of the Microstructure, Hardness and Wear Properties, *Surf. Coat. Technol.*, 2019, **374**, p 1091–1099
10. X.L. Lu, X.B. Liu, P.C. Yu et al., Synthesis and Characterization of Ni60-hBN High Temperature Self-lubricating Anti-wear Composite Coatings on Ti6Al4V Alloy by Laser Cladding, *Opt. Laser Technol.*, 2016, **78**, p 87–94
11. Z. Wu, F. Zhou, K. Chen et al., Friction and Wear Properties of CrSiCN Coatings with Low Carbon Content as Sliding Against SiC and Steel Balls in Water, *Tribol. Int.*, 2016, **94**, p 176–186
12. Q. Shi, H. Zhu, and C. Li, The Effects of the Addition of Ti3SiC2 on the Microstructure and Properties of Laser Cladding Composite Coatings, *Coatings*, 2020, <https://doi.org/10.3390/coatings10050498>
13. W. Chen, B. Liu, L. Chen et al., Effect of Laser Cladding Stellite 6-Cr3C2-WS2 Self-Lubricating Composite Coating on Wear Resistance and Microstructure of H13, *Metals*, 2020, <https://doi.org/10.3390/met10060785>
14. M. Xia, D. Gu, C. Ma et al., Fragmentation and Refinement Behavior and Underlying Thermodynamic Mechanism of WC Reinforcement During Selective Laser Melting of Ni-Based Composites, *J. Alloys Compd.*, 2019, **777**, p 693–702
15. Q.B. Nguyen, Z. Zhu, B.W. Chua et al., Development of WC-Inconel Composites Using Selective Laser Melting, *Arch. Civ. Mech. Eng.*, 2018, **18**, p 1410–1420
16. K. Wang, Y. Liu, Z. Sun et al., Microstructural Evolution and Mechanical Properties of Inconel 718 Superalloy Thin Wall Fabricated by Pulsed Plasma Arc Additive Manufacturing, *J. Alloys Compd.*, 2020, **819**, p 152936
17. M.J. Sohrabi, H. Mirzadeh, and M. Rafiei, Solidification Behavior and Laves Phase Dissolution During Homogenization Heat Treatment of Inconel 718 Superalloy, *Vacuum*, 2018, **154**, p 235–243
18. G.L. Li, Y.L. Li, T.S. Dong et al., Microstructure and Interface Characteristics of NiCrBSi Thick Coating Remelted by TIG Process, *Vacuum*, 2018, **156**, p 440–448
19. Y.L. Li, T.S. Dong, G.L. Li et al., Microstructure Evolution and Properties of NiCrBSi Thick Coating Remelted by Gas Tungsten Arc, *Surf. Coat. Technol.*, 2018, **349**, p 260–271
20. T. Liyanage, G. Fisher, and A.P. Gerlich, Influence of Alloy Chemistry on Microstructure and Properties in NiCrBSi Overlay Coatings Deposited by Plasma Transferred Arc Welding (PTAW), *Surf. Coat. Technol.*, 2010, **205**, p 759–765
21. X. Chen, X. Qin, Z. Zhu et al., Microstructural Evolution and Wear Properties of the Continual Local Induction Cladding NiCrBSi Coatings, *J. Mater. Process. Technol.*, 2018, **262**, p 257–268
22. L. Ren, M. Zhou, T. Lu et al., Eutectic Phase Strengthening and Strain Rate Sensitivity Behavior of AZ80 Magnesium Alloy, *Mater. Sci. Eng., A*, 2020, **770**, p 138548
23. J. Li, S.L. Shrentha, Y. Long et al., The Formation of Eutectic Phases and Hot Cracks in One Ni-Mo-Cr Superalloy, *Mater. Des.*, 2016, **93**, p 324–333
24. D. Ye, C. Du, M. Wu et al., Microstructure and Mechanical Properties of Sn-xBi Solder Alloy, *J. Mater. Sci.: Mater. Electron.*, 2015, **26**, p 3629–3637
25. W. Yu and Q. Hao, The Phase Transformation of $Al_3(Mn, Ni)_2$ Eutectic Phase in an Al-4Ni-2Mn Alloy During Heat Treatment, *Mater. Charact.*, 2017, **129**, p 53–59
26. W. Yu, Q. Hao, and Q. Wang, Phase Transformation Behavior of $Al_3(Mn, Ni)_2$ Eutectic Phase During Heat Treatment at 600 °C in Al-4Ni-2Mn Alloy, *Trans. Nonferr. Met. Soc. China*, 2018, **28**, p 1913–1919
27. Y. Guo, M. Sun, B. Xu et al., A Method Based on Semi-solid Forming for Eliminating Laves Eutectic Phase of INCONEL 718 Alloy, *J. Mater. Process. Technol.*, 2017, **249**, p 202–211
28. V. Anggraini, A. Asadi, A. Syamsir et al., Three Point Bending Flexural Strength of Cement Treated Tropical Marine Soil Reinforced by Lime Treated Natural Fiber, *Measurement*, 2017, **111**, p 158–166
29. S. Sun, H. Fu, X. Ping et al., Reinforcing Behavior and Microstructure Evolution of NbC in Laser Cladded Ni45 Coating, *Appl. Surf. Sci.*, 2018, **455**, p 160–170

30. M. Liu, J. Takagi, and A. Tsukuda, Investigation of Strength Degradation and Strength Recovery via Short Time Heating for Ground Alumina Ceramics with Different Grain Size, *J. Mater. Process. Technol.*, 2004, **145**, p 276–280
31. C. Du, Q. Pan, S. Chen et al., Effect of Rolling on the Microstructure and Mechanical Properties of 6061-T6 DS-FSW Plate, *Mater. Sci. Eng., A*, 2020, **772**, p 138692
32. G.W. Hu, L.C. Zeng, H. Du et al., Tailoring Grain Growth and Solid Solution Strengthening of Single-Phase CrCoNi Medium-Entropy

Alloys by Solute Selection, *J. Mater. Sci. Technol.*, 2020, **54**, p 196–205

Publisher's Note Springer Nature remains neutral with regard to jurisdictional claims in published maps and institutional affiliations.